Microsyst Technol (2011) 17:1009–1023
DOI 10.1007/s00542-011-1250-x

TECHNICAL PAPER

Robust control design for precision positioning of a generic piezoelectric system with consideration of microscopic hysteresis effects

Paul C.-P. Chao · Pen-Yen Liao · Meng-Yen Tsai · Chin-Teng Lin

Received: 31 August 2010 / Accepted: 27 February 2011 / Published online: 18 February 2011
© Springer-Verlag 2011

Abstract This study performs precision positioning of a generic piezoelectric structure against hysteresis effects by finite elements, microscopic hysteresis cancellation and robust H_∞ compensation. The designed control algorithm is expected to be effective in enhancing servo performance of hard disk drives. The precision positioning is accomplished by adding a polarization term into the linear constitutive equations of piezoelectric materials. This polarization term is then described by the well-known Preisach model. Applying basic principles of finite elements and Hamilton's thoery, the macroscopic governing equations of an arbitrary piezoelectric system in finite elements are obtained. Based on the macro-model, a controller consisting of two parts is designed to perform the precision positioning of a generic piezo-structure. The first part is responsible for direct hysteresis cancellation at the microscopic level, while the second one is a robust H_∞ controller to overcome inevitable cancellation errors. In this way, the control effort is then more effective than the conventional PI and double-lead controller without microscopic hysteresis cancellation. A simple piezoelectric structure of a bender-bimorph cantilever beam is considered for designs and experimental validation. Based on experimental results, the proposed control design is found effective to suppress hysteresis effects as opposed to conventional controllers.

P. C.-P. Chao (✉) · M.-Y. Tsai · C.-T. Lin
Department of Electrical Engineering,
National Chiao Tung University, Hsinchu 300, Taiwan
e-mail: pchao@mail.nctu.edu.tw

P. C.-P. Chao
Institute of Imaging and Biomedical Phonics,
National Chiao Tung University, Tainan 711, Taiwan

P.-Y. Liao
Department of Mechanical Engineering,
Chung-Yuan Christian University, Chung-Li 320, Taiwan

1 Introduction

Smart materials have drawn much attention in recent years in areas of sensing and actuation. Among all materials, such as piezoelectric, electrostrictive, electrorheological materials, and shape memory alloys, etc., the piezoelectric materials are most used in variety of sensors and actuators due to simple construction, small size, high sensitivity and precision (Shaffer and Fried 1970; Lee 1979). Known applications include scanning tunneling microscopy, ultrasonic motors, resonators, accelerometers and hard disk drives. However, it is well noted that the actuation behaviors of piezoelectric structures have two major nonlinearities, i.e., hysteresis and creep (Newcomb and Flinn 1982; Chen and Montgomery 1980), undermining the performance of the piezoelectric actuators. The maximum error due to the hysteresis effect can be as much as 10–15% of the actuated distance if the piezoelectric structure is excited in an open-loop fashion (Peng et al. 2010).

For hard disk drives, the piezo-electric actuators have been designed and used for (a) precision positioning for track-following control (Mori et al. 1991; Li and Horowitz 2002; Li et al. 2003; Huang et al. 2006; Oboe et al. 1999; Tsai and Yen 1999; Tokuyama et al. 2001; Lou et al. 2002) or (b) flying height control of the magnetic reading head (Gao and Swei 2000; Liu et al. 2002; Suzuki et al. 2003; Tagawa et al. 2003). For afore-objective (a), the piezo-actuator is usually part of a dual-stage actuator system, which consists of a "fine" microactuator (MA) realized by piezo-structures and a "coarse" voice coil motor (VCM).

For (b), the piezo-actuator could serves as a sole actuator or part of a dual-stage one. Part of reasons for the piezo-actuators being only used in micro-actuators is their inability to achieve long-range precision positioning due to hysteresis. It is evident in some of the previous works (Oboe et al. 1999; Tsai and Yen 1999; Tokuyama et al. 2001; Lou et al. 2002) that the hysteresis effects are still present as a critical factor in achieving required positioning precision. To tackle the hystereis, the control scheme synthesized in the present study aims to offer the potential capability of effectively counteracting the hysteresis effects of the microactuators, and also, extending positioning range of the piezo-MA to ease the burden of the VCM or even utilize the piezo-MA solely to perform the precision positioning.

Research works (Mayergoyz 1991; Ge and Jouaneh 1995; Freeman and Joshi 1995; Hughes and Wen 1995; Yu et al. 2002) had been conducted to prescribe hysteresis effects of piezoelectric structures via casting the lumped input–output relation of piezoelectric device/system into a pre-chosen mathematical models, such as Preisach (Mayergoyz 1991; Preisach 1935; Hutton 2009), Bouc-Wen (Andronikou et al. 1983), Prandtl–Ishlinksii (Dong and Tan 2009; Janaideh et al. 2009) or domain wall (Chen and Wang 1998). These approaches of "macroscopic" modeling on the hysteresis effects requires experimental identification on the parameters of the hysteresis model adopted, whenever a new piezo-structure is considered. To simplify the modeling, a novel microscopic modeling technique on the hysteresis effects was proposed with the aim to incorporate the hysteresis effects in the level of microscopic scales (Simkovics et al. 2000). This is accomplished by adding a polarization term to one of linear constitutive equations for piezoelectric materials. The polarization term is then described by the well-known hysteresis model, Preisach model. Applying basic principles of finite elements and Hamilton's theory, the macroscopic governing equations of an arbitrary piezoelectric system in finite elements can be obtained. Based on the model, a controller consisting of two parts is designed in this study to perform precision positioning of a generic piezo-structure. The first part is responsible for a direct cancellation of the hysteresis term at the microscopic level, while the second one is a robust H_∞ controller responsible to overcome the errors of the aforementioned hysteresis cancellation. In this way, the control effort is more effective than the conventional PI and double-lead controller (Kim et al. 2009) without microscopic hysteresis cancellation. A typical piezoelectric structure of bender-bimorph cantilever beam is considered for designs and experimental validation. General closeness is found between the simulations and experimental data. Furthermore, the designed controller is found effective in experiments to suppress hysteresis effects and achieve excellent precision positioning.

The remainder of this paper is organized as follows. In section two, linearized piezoelectric constitutive equations are modified with an addition of the polarization prescribed by Preisach model. Section three proposes finite element modeling with an exemplary demonstration of a piezoelectric bimorph beam. Section four presents experimental studies to verify the effectiveness of the proposed modeling technique.

2 Modified constitutive equations

Based on the principle of virtual displacement, the internal mechanical stress $\mathbf{T}$ varied by the virtual strains $\delta\mathbf{S}$ in piezoelectric materials must be equal to the external forces R applied on the considered region Ω, yielding

$$\int_{\Omega} T_{ij}\delta S_{ij} d\Omega = R. \tag{1}$$

On the other hand, the dielectric displacement $\mathbf{D}$ varied by the virtual electric field strength $\delta\mathbf{E}$ is equal to electric charges Q accumulated in the considered volume, yielding

$$\int_{\Omega} D_i\delta E_i d\Omega = Q. \tag{2}$$

The above equations (1, 2) are commonly assumed coupled by linear piezoelectric material relations

$$\begin{aligned} \mathbf{T} &= c^E\mathbf{S} - e^t\mathbf{E}, \\ \mathbf{D} &= e\mathbf{S} + \varepsilon^S\mathbf{E}, \end{aligned} \tag{3}$$

where c^E contains elastic moduli, e^t and e are piezoelectric coefficients and ε^S are dielectric constants or permittivities. It is known that application of strong electric fields and large mechanical stress to piezoelectric materials leads to switchings of electric orientations of ferroelectric grains (dipoles) inside the materials. The phenomenon is known as "polarization," as illustrated by Fig. 1. While polarizing, certain amount of energy is consumed to make possible re-orientation of grains, leading to the difference in the load-response relations with ascending and descending loads. This is known as ferroelectric hysteresis. To reflect the effects of ferroelectric hysteresis, one can add an additional term $\hat{\alpha}\mathbf{P}$ proportional to dielectric polarization $\mathbf{P}$ into the second equation in Eq. 3, yielding

$$\begin{aligned} \mathbf{T} &= c^E\mathbf{S} - e^t\mathbf{E}, \\ \mathbf{D} &= e\mathbf{S} + \varepsilon^S\mathbf{E} + \tilde{\alpha}\mathbf{P}(\mathbf{E}), \end{aligned} \tag{4}$$

where $\tilde{\alpha}$ represents the electric displacement change due to unit polarization. With the modified constitutive equations

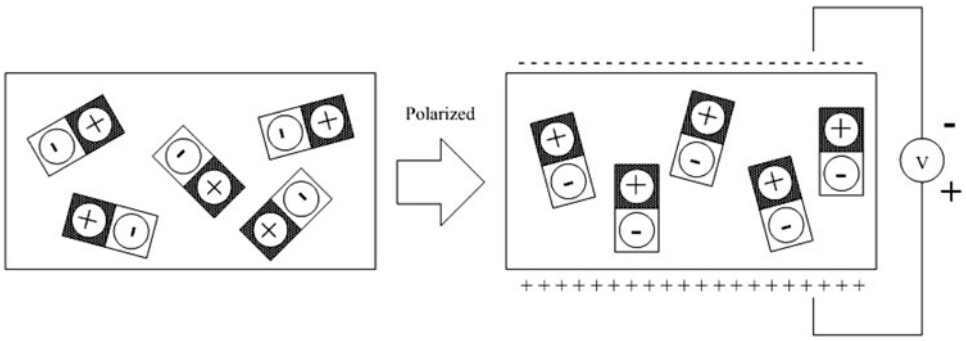

Fig. 1 Illustration of polarization

(4) in hand, the hysteresis effects due to varied input electric field **E** are in fact characterized in microscopic level as the changes in polarization **P**(**E**) in Eq. 4.

3 Preisach model for polarization

The effects of ferroelectric hysteresis had shown high similarity with ferromagnetic material behavior. Therefore, the Preisach model (Mayergoyz 1991), which is commonly used to describe ferromagnetic hysteresis, is adopted herein to prescribe the polarization term **P**(**E**) in Eq. 4. Besides Preisach, other microscopic models effectively describing the hysteresis can also be used herein to model **P**(**E**), like Prandtl–Ishlinksii model in Janaideh et al. (2009). Utilizing the Preisach modeling technique, each polarization term in **P**(**E**) in Eq. 4 can be expressed as functions of the corresponding applied electric field E by the integral

$$P(t) = \iint_{\alpha \geq \beta} \mu(\alpha, \beta)\gamma_{\alpha\beta}[E(t)]d\alpha d\beta, \tag{5}$$

where $\gamma_{\alpha\beta}$ is the elementary operator as shown in Fig. 2, which is also a function depending on E. $\gamma_{\alpha\beta}$ varies from zero to one, emulating an on–off to distinguish the change in input E either in ascending or descending for reflecting the hysteresis effect. The rule of the dependence of $\gamma_{\alpha\beta}$ on E follows the illustration in Fig. 3, where α and β are maximum and minimum input values of E. $\mu(\alpha, \beta)$ in Eq. 5 is in fact a function of α and β, so-called Preisach function, which captures a variety of different hysteresis characteristics with given values of α and β, corresponding switching values of E between ascending and descending. For a certain piezoelectric material, if $\mu(\alpha, \beta)$ is known, the polarization due to hysteresis can be calculated directly by the integration in Eq. 5. However, since determination of the weighting function $\mu(\alpha, \beta)$ requires double differentiation which may amplify the errors in experimental data, another approach (Mayergoyz 1991) is used for numerical implementation of the Preisach function. Also, $\mu(\alpha, \beta)$ in Eq. 5 could be in varied forms to model asymmetric hysteresis loops and saturated hysteresis output, as handled by Prandtl–Ishlinksii model in (Janaideh et al. 2009). The numerical method to calculate $P(t)$ is stated as follows.

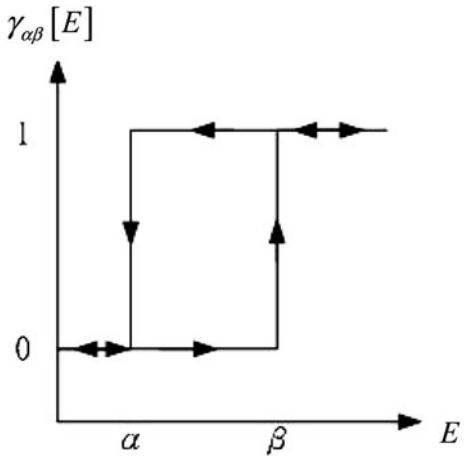

Fig. 2 Elementary hysteresis operator

For the case of monotonically increasing input $E(t)$ at the final state, $P(t)$ is in fact a double integral of the weighting function $\mu(\alpha, \beta)$ on a region that is circumscribed by a set of interface links whose final segment is horizontal (see Fig. 3a, c). Here, the integration is equivalent to the sum of trapezoids within this region $S^+(t)$. Thus, the general formula for estimating the piezoelectric expansion, when the input $E(t)$ is monotonically increasing at the final state, is

$$P(t) = \sum_{k=1}^{n} \left[F\left(\alpha'_k, \beta'_{k-1}\right) - F\left(\alpha'_k, \beta'_k\right)\right] + F\left[E(t), \beta'_n\right], \tag{6}$$

where function F is a double integral of the weighting $\mu(\alpha, \beta)$ over the shaded region in the (β, α) plane as shown in Fig. 3c. Similarly, for the case of monotonically decreasing input $E(t)$ at the final state (see Fig. 3b, d), since the integration is equivalent to the sum of the trapezoids within the region $S^+(t)$ in Fig. 3d, the piezoelectric expansion is as following

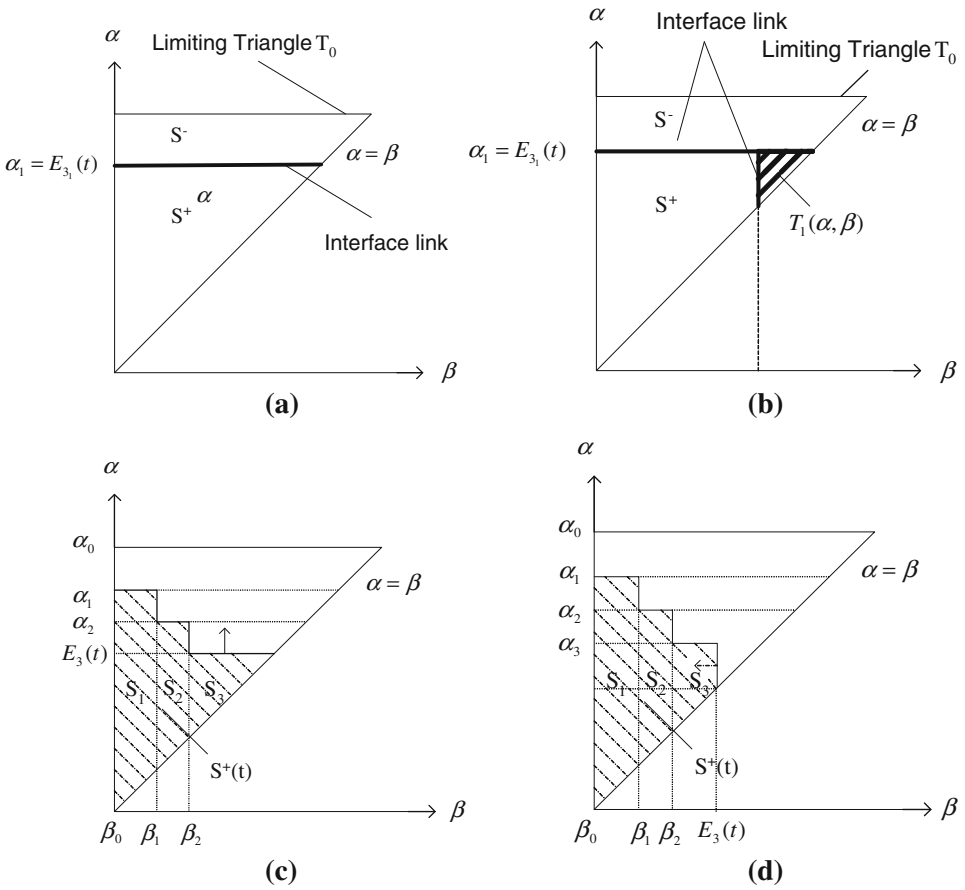

Fig. 3 **a** Links with monotonically increasing input voltage $E_3(t)$, **b** links with monotonically decreasing input $E_3(t)$, **c** the region $S^+(t)$ whose final input is monotonically increasing, **d** the region $S^+(t)$ whose final input is monotonically decreasing

$$P(t) = \sum_{k=1}^{n-1}\left[F(\alpha'_k,\beta'_{k-1}) - F(\alpha'_k,\beta'_k)\right] + \left[F(\alpha'_n,\beta'_{n-1}) - F(\alpha'_n,E(t))\right]. \tag{7}$$

With Eqs. 6–7 in hand, the microscopic polarization P can be captured via prior identification for the dependence of polarization F on $\{\alpha, \beta\}$ based on macroscopic experimental data and using the technique of finite element modeling, in later sections. This identification procedure is realized by (1) sampling the (β, α) plane as in Fig. 4, (2) experimentally recording the correspondence between sampled (α, β)'s and F's from measurements, and finally (3) interpolating the values of F's within sampled (α, β)'s using

$$F(\alpha,\beta) \cong c_0 + c_1\alpha + c_2\beta + c_3\alpha\beta, \tag{8}$$

$$F(\alpha,\beta) \cong c_4 + c_5\alpha + c_6\beta, \tag{9}$$

for square and triangular areas, respectively, shown in Fig. 4. With the above F identified; i.e., c_i's in Eqs. 8, 9 are determined, the polarization $P(t)$ either in ascending or descending branches at final state, as shown in Eqs. 6, 7, respectively, can be computed. Note that the identification process is based on macroscopic experimental data and the equations of motion built from finite element modeling in the next section.

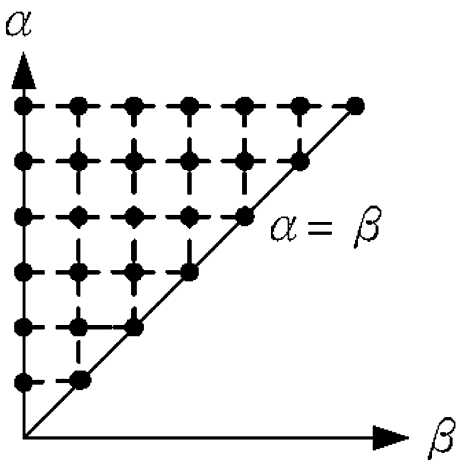

Fig. 4 Sampled points on a discretized (β, α) plane

4 Finite element modeling

A simple bimorph piezoelectric beam as depicted and photographed in Fig. 5 is considered for demonstrating the

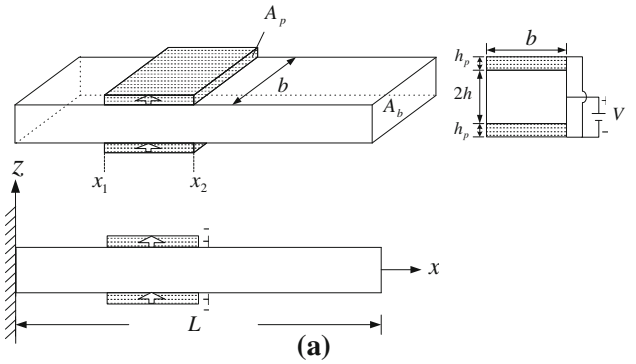

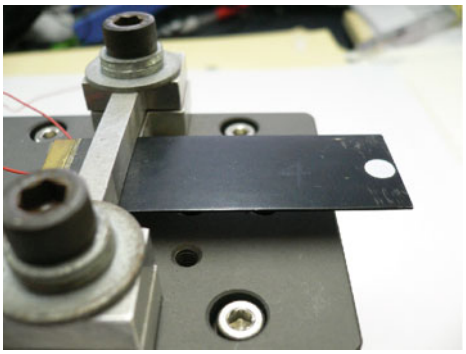

Fig. 5 **a** Schematic diagram of the cantilever beam with two piezoelectric layers bounded on the *top* and *bottom*, where the input voltage V is applied between the intermediate electrode and the *top*/*bottom* electrodes, **b** photograph of the piezoelectric beam considered for the experiment

afore-proposed microscopic modeling on hysteresis effects, which are seen as results of microscopic polarization. A subsequent system modeling based on finite elements is conducted to reflect hysteresis effects in macroscopic level. As shown in Fig. 5a, the considered piezo-beam owns length L, width b, and a pair of piezoelectric patches extending from $x = x_1$ to x_2 in parallel polarizations. The thicknesses of the beam and piezo-electric patches are $2h$ and h_p, respectively. Assuming small slenderness ratio, Euler beam theory is employed to model the cantilever beam. The modeling process starts with a special case and alternative representation of the constitutive Eqs. 4 as

$$\begin{aligned} \sigma_{11} &= E_p \varepsilon_{11} - h_{31} D, \\ E_3 &= -h_{31} \varepsilon_{11} + \beta_{33} D + \hat{\alpha} P(E_3), \end{aligned} \tag{10}$$

where 1 and 3 refer to directions of x and z in Fig. 5a, respectively, and $\hat{\alpha}$ denotes the electric field change due to unit polarization. Also in Eqs. 10, σ_{11} and ε_{11} are the stress and strain in the x direction of piezoelectric elements; h_{31} and β_{33} are the piezoelectric and dielectric constants, respectively; E_p is Young's modulus of piezoelectric material. Potential and kinetic energies are next formulated

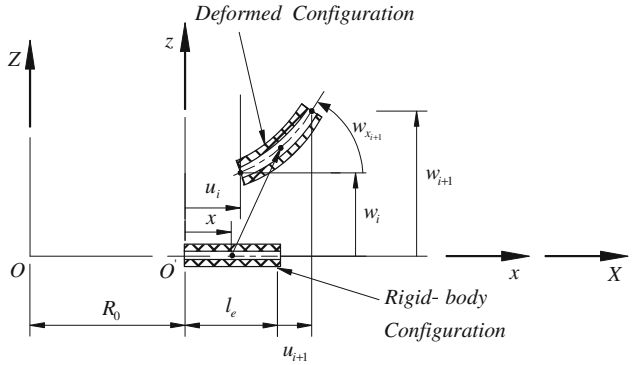

Fig. 6 Deformation of the ith element of the beam

for application of Hamilton's equations to derive equations of motion. The proposed procedure of finite element modeling can easily be extended to arbitrary piezoelectric structures with hysteresis effects via establishing the polarization term P in Eqs. 10.

The finite element modeling for the piezo-beam starts with considering deformation for the ith element of the beam as shown in Fig. 6, where R_0 is the distance from origin O of the global coordinate system to the origin O' of the local coordinate system. The displacements of the Euler beam in the x- and z-direction are, respectively,

$$u_1(x,t) = u(x,t) - z w_x(x,t), \tag{11a}$$

$$u_2(x,t) = 0, \tag{11b}$$

$$u_3(x,t) = w(x,t), \tag{11c}$$

where $u(x, t)$ and $w(x, t)$ represent axial and transverse displacements, respectively; moreover the subscript x denotes the spatial derivative with respect to x. The position vector of an arbitrary point located on the neutral axis after deformation is

$$\mathbf{R}(x,z,t) = (x + u - z w_x)\,\mathbf{i} + (z + w)\,\mathbf{k}. \tag{12}$$

The total kinetic energy of the piezoelectric bender-bimorph beam consisting of one beam and two piezoelectric patches as shown in Fig. 5a is

$$\begin{aligned} T &= T_b + T_p \\ &= \int_{V_b} \frac{1}{2}\rho_b \mathbf{R}_t \cdot \mathbf{R}_t d\mathrm{V}_b + \int_{V_p} \frac{1}{2}\rho_p \mathbf{R}_t \cdot \mathbf{R}_t d\mathrm{V}_p|_{up} + \int_{V_p} \frac{1}{2}\rho_p \mathbf{R}_t \cdot \mathbf{R}_t d\mathrm{V}_p|_{down} \\ &= \frac{1}{2}\int_0^L \rho_b A_b (u_t^2 + w_t^2)\,dx + \int_{x_1}^{x_2} \rho_p A_p (u_t^2 + w_t^2)\,dx \end{aligned} \tag{13}$$

where subscripts t denotes time differentiation; ρ_b and ρ_p are the mass densities of the beam and piezoceramics, respectively. Also, the cross section areas for beam and piezo-patches are $A_b = 2hb$ and $A_p = h_p b$, respectively; V_b and V_p are volumes of beam and piezo-patches, respectively; $2h$ is the height of the beam; b is its width. The linear Lagrangian strains of Euler beam are

$$\varepsilon_{11} = u_x - zw_{xx}, \quad \varepsilon_{12} = 0, \quad \varepsilon_{13} = \varepsilon_{31} = w_x. \tag{14}$$

On the other hand, the potential energy is

$$\begin{aligned} U &= U_b + U_p, \\ &= \frac{1}{2}\int_{V_b} \sigma_{11}\varepsilon_{11} dV_b + \frac{1}{2}\int_{V_p} (\sigma_{11}\varepsilon_{11} + DE_3) dV|_{upper} \\ &\quad + \frac{1}{2}\int_{V_p} (\sigma_{11}\varepsilon_{11} + DE_3) dV|_{lower} \\ &= \frac{1}{2}\int_0^L [E_b A_b u_x^2 + E_b I_b w_{xx}^2] dx \\ &\quad + \frac{1}{2}\int_{x_1}^{x_2} [E_p A_p u_x^2 - E_p A_p u_x w_{xx}(2h + h_p) \\ &\quad + E_p I_p w_{xx}^2 - 2h_{31} A_p D u_x \\ &\quad + h_{31} A_p D w_{xx}(2h + h_p) + A_p \beta_{33} D^2 - A_p \hat{\alpha} P D] dx, \end{aligned} \tag{15}$$

where I_b and I_p are the moments of inertia about the neutral axis of the beam and piezoelectric layer, respectively. The virtual work done by the applied voltage V on the piezo-actuators can be expressed as

$$\delta W = 2\int_{x_1}^{x_2} V \delta D b dx, \tag{16}$$

where the input voltage V is applied across the total thickness of the piezo-patches as shown in Fig. 5a. Using Hamilton's principle,

$$\int_{t_1}^{t_2} \delta(T - U + W)\, dt = 0, \tag{17}$$

one obtains the governing equations in axial interval $[0, L]$ as follows,

$$\begin{aligned} u: \quad & -(\rho_b A_b + 2\rho_p A_p) u_{tt} + (E_b A_b + 2E_p A_p) u_{xx} \\ & - \frac{1}{2} E_p A_p (2h + h_p) w_{xxx} = 0, \end{aligned} \tag{17a}$$

$$\begin{aligned} w: \quad & -(\rho_b A_b + \rho_p A_p) w_{tt} - (E_b A_b + E_p A_p) w_{xxxx} \\ & + \frac{1}{2} E_p A_p (2h + h_p) u_{xxx} = 0, \end{aligned} \tag{17b}$$

$$\begin{aligned} D: \quad & h_{31} A_p u_x - \frac{1}{2} h_{31} A_p w_{xx}(2h + h_p) - A_p \beta_{33} D \\ & + \frac{1}{2} A_p \hat{\alpha} P + V b_p = 0. \end{aligned} \tag{17c}$$

Note in the above equations that the piezoelectric-related terms, with subscript p, only exist in the interval $[x_1, x_2]$, where the beam structure does not exist. Based on Eq. 17c, the electric displacement can be derived as

$$D = \frac{V b_p + h_{31} A_p u_x - \frac{1}{2} h_{31} A_p w_{xx}(2h + h_p) + \frac{1}{2} A_p \hat{\alpha} P}{A_p \beta_{33}}. \tag{18}$$

The clamped-free boundary conditions at $x = 0$ and $x = L$ of the piezo-beam in Fig. 5a, respectively, are

$$\begin{aligned} & u(0,t) = 0, \quad w(0,t) = 0, \quad w_x(0,t) = 0, \\ & u_x(L,t) = 0, \quad w_{xx}(L,t) = 0, \quad w_{xxx}(L,t) = 0. \end{aligned} \tag{19}$$

With potential/kinetic energies and boundary conditions in hands, the finite element modeling can then be performed by expressing the energies (13, 15) in terms of nodal coordinates and then derive the equations of motion. This process starts with substituting expression (18) into (13, 15) for eliminating the dependence of potential and kinetic energies on the electric displacement D. In the next step, as shown in Fig. 7, a set of $(N_e + 1)$ equally-spaced nodes along the axial, neutral axis of the beam, x, are selected to build N_e beam elements. Within the axial range from $x = x_1$ to x_2, there are also nodes associated with piezoelectric patches. Note that three degrees of freedom are associated with each node; i.e., $\{u_i,\ w_i,\ w_{x,i}\}$. Assuming cubic interpolation functions between degrees of freedom of adjacent nodes, one is able to express the dynamic states of an arbitrary axial location within the ith element based on the beam theorem, yielding

$$\mathbf{q}_i = \mathbf{N}_{i,u}^{e\,T} \mathbf{u}_i + \mathbf{N}_{i,w}^{e\,T} \mathbf{w}_i \tag{20}$$

where

$$\begin{aligned} & \mathbf{q}_i \equiv [\,u_i \quad w_i \quad w_{x_i} \quad u_{i+1} \quad w_{i+1} \quad w_{x_{i+1}}\,]^T; \\ & \mathbf{u}_i = [\,u_i \quad 0 \quad 0 \quad u_{i+1} \quad 0 \quad 0\,]^T; \mathbf{w}_i = [\,0 \quad w_i \quad w_{x_i} \quad 0 \quad w_{i+1} \quad w_{x_{i+1}}\,]^T; \\ & \mathbf{N}_{i,u}^e = [N_{u_1} \quad 0 \quad 0 \quad N_{u_2} \quad 0 \quad 0]^T; \mathbf{N}_{i,w}^e = [0 \quad N_{w_1} \quad N_{w_2} \quad 0 \quad N_{w_3} \quad N_{w_4}]^T; \\ & N_{u_1} = 1 - \frac{\hat{x}}{s}; N_{u_2} = \frac{\hat{x}}{s}; N_{w_1} = \frac{1}{s^3}[2\hat{x}^3 - 3\hat{x}^2 s + s^3]; N_{w_2} = \frac{1}{s^3}[\hat{x}^3 s - 2\hat{x}^2 s^2 + \hat{x} s^3]; \\ & N_{w_3} = \frac{1}{s^3}[-2\hat{x}^3 + 3\hat{x}^2 s]; N_{w_4} = \frac{1}{s^3}[\hat{x}^3 s + \hat{x}^2 s^2]. \end{aligned}$$

Note in the above equations that s is the axial length of the ith beam element; $\hat{x}$ is the local axial coordinate; the superscript e for $\mathbf{N}_i^e$'s indicates that these interpolations are in local dimension. The potential and kinetic energies in

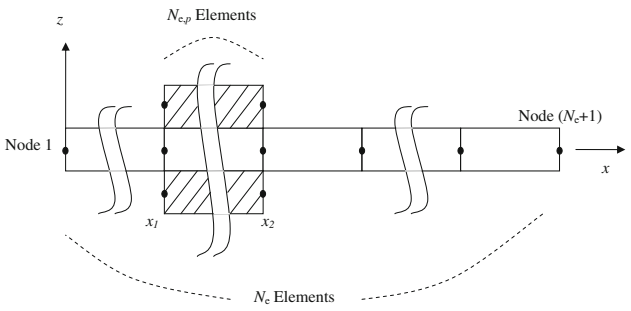

Fig. 7 The elements and nodes of the piezo-beam from side view of Fig. 5a

Eqs. 13, 15 are next re-represented as sum of those sub-energies corresponding to each element. Expressing these sub-energies in terms of nodal coordinates $\{u_i, w_i, w_{x,i}\}$'s based on Eq. 20 and assembling sub-energies, one is able to derive kinetic and potential energies in terms of newly-defined nodal coordinates. Based on the correspondence in the mass, damping and stiffness matrices between assembled energies and bulk energies in a standard dynamic system, one can derive

$$\mathbf{M}\ddot{\mathbf{Q}} + \mathbf{C}\dot{\mathbf{Q}} + \mathbf{K}\mathbf{Q} = \mathbf{F}, \tag{21}$$

where

$$Q \equiv \begin{bmatrix} u_1 & w_1 & w_{x,1} & \dots & u_{N_e+1} & w_{N_e+1} & w_{x,N_e+1} \end{bmatrix}^T$$

$$\mathbf{M} = \sum_{k=1}^{N_e} \left\{ \int_0^s \rho_b \left[\left(A_b \mathbf{N}_{k,u}^T \mathbf{N}_{k,u} + I_b \mathbf{N}_{k,w_x}^T \mathbf{N}_{k,w_x} \right) + A_b \mathbf{N}_{k,w}^T \mathbf{N}_{k,w} \right] dx \right\} + \sum_{k_p=1}^{N_{e,p}} \left\{ \int_0^s 2\rho_p \left[\left(A_p \mathbf{N}_{k_p,u}^T \mathbf{N}_{k_p,u} + I_p \mathbf{N}_{k_p,w_x}^T \mathbf{N}_{k_p,w_x} \right) + A_p \mathbf{N}_{k_p,w}^T \mathbf{N}_{k_p,w} \right] dx \right\}, \tag{21a}$$

$$\mathbf{K} = \sum_{k=1}^{N_e} \left\{ \int_0^s E_b \left(A_b \mathbf{N}_{k,u_x}^T \mathbf{N}_{k,u_x} + I_b \mathbf{N}_{k,w_{xx}}^T \mathbf{N}_{k,w_{xx}} \right) \right\} dx + \sum_{k_p=1}^{N_{e,p}} \left\{ \int_0^s 2E_p \left[A_p \mathbf{N}_{k_p,u_x}^T \mathbf{N}_{k_p,u_x} + I_p \mathbf{N}_{k_p,w_{xx}}^T \mathbf{N}_{k_p,w_{xx}} \right] - \frac{h_{31}^2 A_p (h+h_p)^2}{\beta_{33}} \mathbf{N}_{k_p,w_{xx}}^T \mathbf{N}_{k_p,w_{xx}} dx \right\}, \tag{21b}$$

$$\mathbf{F} = -\sum_{k_p=1}^{N_{e,p}} \left\{ \int_0^s \frac{h_{31}(2b_p V + A_p \hat{\alpha} P)(h+h_p)}{2\beta_{33}} N_{k_p,w_{xx}} \right\} dx, \tag{21c}$$

where $\mathbf{N}_i$'s are global versions of $\mathbf{N}_i^e$'s defined in Eqs. 20; i.e., each column vector $\mathbf{N}_i$ is an extension of the corresponding $\mathbf{N}_i^e$ to full system dimension with zeros at the entries not related the ith element. In addition, k_p is the summation index for those elements of piezoelectric elements, while $N_{e,p}$ is the total number of piezoelectric elements. In the final step of finite element modeling, boundary conditions (19) at node 1 and $(N_e + 1)$ are applied. Furthermore, the nodes for beam and piezo-patches at the same axial position are assumed identical dynamical states for continuity, leading to the equations of motion in the dimensions of $3(N_e - 1)$. It is seen from Eqs. 21, 21c that the microscopic hysteresis effect due to polarization P is incorporated in the term of $A_p\hat{\alpha}P$, acting as a modification on the piezoelectric actuation by the applied voltage V in the level of macroscopic behaviors. This finding enables identification of microscopic polarization P through macroscopic experimental data of beam responses, as conducted in the following section.

5 Polarization identification

With the system equations of motion established in Eqs. 21 and the piezoelectric force term in Eq. 21c, the microscopic polarization "$\hat{\alpha}P$" as a function of applied voltage V is identified based on macroscopic experiment data in this section. To this end, a series of pre-designated voltages are applied in a quasi-static fashion to the piezoelectric beam, with the aim not to trigger system dynamics. In this way, the system equations 21 is well approximated by

$$\mathbf{K}\mathbf{Q} = \mathbf{F}, \tag{22}$$

where the piezoelectric force $\mathbf{F}$ can be carried out based on integration (21c), yielding

$$\mathbf{F} = \mathbf{c}_F \left(V + \frac{1}{2} h_p \hat{\alpha} P(V) \right) \tag{23}$$

where $\mathbf{c}_F$ is a $3(N_e - 1)$ column vector with constant entries resulted from the integration. With Eqs. 22 and 23, the identification on polarization $\hat{\alpha}P(V)$ in Eq. (23) can be achieved by applying a series of applied voltage and recording piezo-beam reflections corresponding to the DOFs in $\mathbf{Q}$. For maximum sensitivity, the beam tip vertical deflection; i.e., w_{x,N_e+1}, is selected to collect data for identifying $\hat{\alpha}P(V)$ in Eq. 23.

A simple experimental piezo-cantilever beam system as shown in Fig. 5 is set up with the piezoceramic patches in model no. of APC-856 (American Piezo Ceramics 1775). The material properties and dimensions of these piezo-creamic patches, and brass are listed in Table 1. A set of voltages corresponding to intersections in Fig. 8 are applied to the piezo-beam and their resulted tip vertical displacements are listed in Table 2. Based on these data, the interpolation functions in Eqs. 8, 9 can be approximated well for those square and triangular areas in Fig. 8; thus, identifying the polarization $\hat{\alpha}P(V)$ in Eq. 21c. Figure 9 show resulted errors and corresponding error percentages in predicting polarization based on the identified $\hat{\alpha}P(V)$, where it is seen from subfigure (a) that the errors at the intersections of grids are zeros since the

Table 1 Material properties and dimensions of APC-85

	Brass	Piezoceramics
Young's modulus E (N/m^2)	11×10^{10}	5.8×10^{10}
Density ρ (kg/m^3)	8,940	7,500
h_{31} (N/Coulomb): β_{31} (V − m/Coulomb)		-4.698×10^8 3.115×10^7
Total length L (mm)	50	50
Width b (mm)	20	20
Thickness t (mm)	0.36	0.24

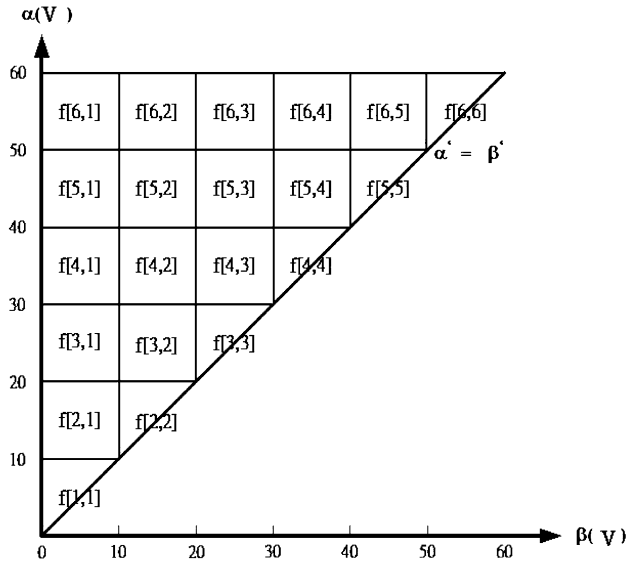

Fig. 8 Discretized β–α plane for experimental identification

Table 2 Measured piezo-beam tip displacements at sampled intersections in Fig. 8

60 (volt)	62.012	201.54	331.76	446.48	561.21	685.23	855.76
50	40.308	173.63	303.86	415.48	514.7	648.02	0
40	31.006	155.03	279.05	381.37	489.89	0	0
30	21.704	130.22	244.95	356.57	0	0	0
20	12.402	117.82	229.44	0	0	0	0
10	9.3018	105.42	0	0	0	0	0
0	0	0	0	0	0	0	(μm) 0
α_i	0	10	20	30	40	50	60
β_i							(volt)

corresponding predictions of polarization $\hat{\alpha}P(V)$ are directly obtained from experiments for interpolations. They are free of interpolation errors. It is also seen from subfigure (b) that the maximum value of error percentages in polarization is controlled under 3% except for the points near the origin. These errors are not of much concern since the hysteresis effects are not significant as subjected to smaller applied voltages.

6 Control design

A control scheme is synthesized in this section to perform precision positioning of a generic piezo-structure. The design process starts with transforming the system equations (21) to those in modal coordinates (Rao 1986). This is accomplished by introducing the modal transformation

$$\mathbf{Q} = \mathbf{U}\boldsymbol{\eta}, \tag{24}$$

where $\mathbf{U}$ is the modal transformation matrix; $\boldsymbol{\eta}$ are modal coordinates. The modal matrix $\mathbf{U}$ is a square matrix whose columns are eigenvectors of the system. Using the modal transformation (24) and performing subsequent standard manipulation, the equations of motion (21) can then be expressed as

$$\ddot{\boldsymbol{\eta}}_i + 2\zeta_i\omega_i\dot{\boldsymbol{\eta}}_i + \omega_i^2\boldsymbol{\eta}_i = -\mathbf{u}_i^T\mathbf{F}, \quad \text{for } i = 1, 2, \ldots, \tag{25}$$

where ζ_i is the damping ratio and ω_i is the natural frequency of the ith mode. To simplify the ensuing design, the modal equations (25) are truncated to the first n equations and, furthermore, represented in a state-space form as

$$\begin{aligned} \dot{\mathbf{x}} &= \mathbf{A}\mathbf{x} + \mathbf{B}\left[V + \frac{1}{2}h_p\hat{\alpha}P(V)\right], \\ y &= \mathbf{C}\mathbf{x}, \end{aligned} \tag{26}$$

where

$$\mathbf{x} = [\eta_1\ \dot{\eta}_1 \cdots \eta_n\ \dot{\eta}_n],$$
$$\mathbf{A} = \begin{bmatrix} 0 & 1 & & & \\ -\omega_n^2 & -2\zeta_n\omega_n & & & \\ & & \ddots & & \\ & & & 0 & 1 \\ & & & -\omega_n^2 & -2\zeta_n\omega_n \end{bmatrix}, \mathbf{B} = \begin{bmatrix} 0 \\ -\mathbf{u}_1^T\mathbf{F} \\ \vdots \\ 0 \\ -\mathbf{u}_n^T\mathbf{F} \end{bmatrix}, \tag{27}$$

and $\mathbf{C}$ is determined based on the system outputs to be controlled. If the controller is designed to perform precision positioning of the piezo-beam tip, $\mathbf{C} = \hat{\mathbf{C}}_o\hat{\mathbf{U}}$ where $\hat{\mathbf{U}}$ is responsible for truncated modal transformation and $\hat{\mathbf{C}}_o = [0 \quad \ldots \quad 0 \quad 1 \quad 0]$.

It appears in system equations (26) that the control effort; i.e., the applied voltage V, generates a nonlinear term due to hysteresis polarization, $\frac{1}{2}h_p\hat{\alpha}P(V)$, in addition to the linear term V. To overcome the hysteresis, a controller consisting of two parts is designed as

$$V = \hat{V} - \frac{1}{2}h_p\hat{\alpha}\hat{P}(V), \tag{28}$$

where $\hat{\alpha}\hat{P}(V)$ cam be obtained from the previously established and identified Preisach model. Note that $\hat{\alpha}\hat{P}(V)$ still deviates slightly from the realistic polarization $\hat{\alpha}P(V)$, as shown in the last section. It is intended in this study that the second term in control law (28) is responsible for a direct cancellation of the actual hysteresis term, $\hat{\alpha}P(V)$ at the microscopic level in Eq. 10, while the first term would be designed via H_∞ control theory to overcome the

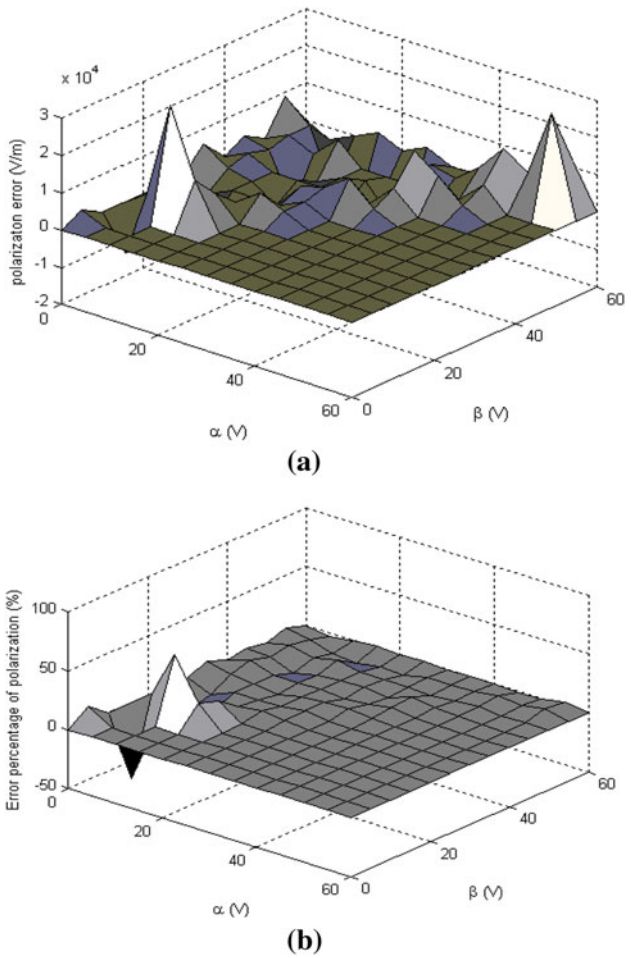

Fig. 9 **a** Error in predicted polarizations over the β–α domain, **b** error percentage

errors of microscopic hysteresis cancellation; i.e., $(P(V)-\hat{P}(V))$. In this way, the control effort is then expected to be more effective and energy-economic than designing a direct control scheme without microscopic hysteresis cancellation. The control law in Eq. 28 leads to a new form of system equations 26 as

$$\begin{aligned}\dot{\mathbf{x}} &= \mathbf{A}\mathbf{x} + (\mathbf{B}+\Delta\mathbf{B})\hat{V},\\ y &= \mathbf{C}\mathbf{x},\end{aligned} \tag{29}$$

where

$$\Delta\mathbf{B} = \mathbf{B}\left(\frac{1}{2}h_p\hat{\delta}\right),\ \hat{\delta} = \hat{\alpha}\left[P(V)-\hat{P}(V)\right]/\hat{V} \tag{29a}$$

With formulation (29), the system uncertainty arising from modeling error of the identified Preisach model, $\hat{\delta}$, can be treated as an additive uncertainty to the controlled system. The system plant G in the frequency domain is then a sum of nominal and uncertain parts, namely G_0 and ΔG, respectively, yielding

$$G = G_0 + \Delta G, \tag{30}$$

where the transfer functions

$$G_0 = \mathbf{C}(s\mathbf{I}-\mathbf{A})^{-1}\mathbf{B}, \tag{31a}$$

$$\Delta G = \mathbf{C}(s\mathbf{I}-\mathbf{A})^{-1}\Delta\mathbf{B}. \tag{31b}$$

To apply a standard H_∞ control design, ΔG is further modeled by $\Delta G = W_a\Delta_a$, where $|\Delta_a| \le 1$. The transfer function of W_a can be derived based on measured modeling error of the identified Preisach model, $\hat{\delta}$, and computed ΔG via Eqs. 29a and 31b, respectively. The upper bounds of the modeling error ΔG over all frequencies can well be approximated by

$$W_a = \frac{3.0795(s+975.2)\left(s^2+659s+1.593\times10^6\right)}{(s+7117)(s^2+62.17s+4.164\times10^5)}. \tag{32}$$

With uncertainty modeled and identified, the system block diagram can be represented by Fig. 10, where the exogenous inputs and controlled outputs are regulated by four weighting functions. e is the error signal; $\hat{u} = V$ is the controlled signal; n is the noise signal; u is the control input; r is the reference signal; G_0 is the nominal plant; K is the controller; W_e is used to reflect the requirements on control objective; W_u does some restrictions on the control or actuator signals; W_n reflect dynamic characteristics of noises. A typical design process of H_∞ control design is initialized by determining the aforementioned weighting functions, which would affect the system sensitivity function, control sensitivity function and complementary sensitivity functions that are used to examine whether or not the originally-set performance specifications are satisfied. The determination of weighting functions for the considered piezo-beam as shown in Fig. 5 is stated in the followings. First, to satisfy the common criterion for stability and performance requirement; i.e., $\|W_eS\|_\infty \le 1$, where S is the sensitivity function, W_e is designed of the form

$$W_e = \frac{s/M_s+\omega_b}{s+\omega_b\varepsilon_e}, \tag{33}$$

where M_s and ω_b are determined by required natural frequency and damping ratio of the controlled system,

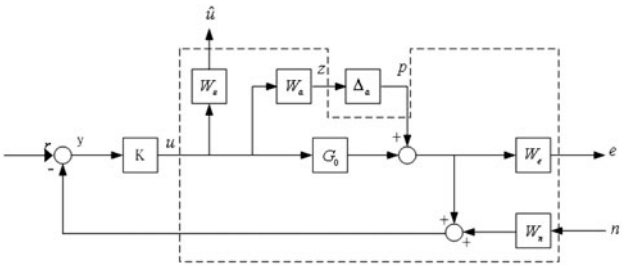

Fig. 10 System block diagram

denoted by ω_n and ζ, respectively. The determination follows

$$\omega_b \approx \omega_n/\sqrt{2},\ \Omega = \sqrt{0.5 + 0.5\sqrt{1+8\zeta^2}},\ \omega_{\max} = \Omega\omega_n,$$

$$M_s := \|S\|_\infty = |S(j\omega_{\max})| = \frac{\Omega\sqrt{\Omega^2+4\zeta^2}}{\sqrt{(1-\Omega^2)^2+4\zeta^2\Omega^2}}.$$

Second, weighting W_u is designated such that $(1/W_u)$ successfully bound $|KS|$ over low and high frequency. This is to reflect saturation limit of the piezo-actuator and its bandwidth. In this way, the weighting can be designed of the form

$$W_u = \frac{s + \omega_{bc}/M_u}{\varepsilon_u s + \omega_{bc}}, \tag{34}$$

where M_u is designated as 60, which is the maximum input voltage to the piezoelectric beam considered in this study, while the bandwidth frequency of the beam, $\omega_{bc} = 1,000\,(\text{rad/s})$, is designated as the controller bandwidth. In the next step, a suitable ε_u is to be chosen to satisfy $\|W_u KS\|_\infty \le 1$ by the small gain theorem (Zhou and Doyle 1998), which is set as 0.05. Third, weighting W_n is used to incorporate sensor noise that is relatively significant in the ranges of high frequencies. Therefore, W_n is determined as a form of a high-pass filter as

$$W_e = \frac{s}{s + \omega_{nc}}, \tag{35}$$

where ω_{nc} is the cut-off frequency of the sensor. In this study, where laser interferometers are used to measure the piezo-beam tip motion, simple experiments show that the cuff-off frequency is around 60 Hz. Having determined all transfer functions in the blocks in Fig. 10, following the common procedure of H_∞ control design, the last step is to convert the system blocks in Fig. 10 into that in Fig. 11 via linear fractional transformation (LFT) (Zhou and Doyle 1998). Through some simple algebraic manipulations, one can obtain

$$\begin{bmatrix} z \\ \hat{u} \\ e \\ y \end{bmatrix} = \mathbf{M}(s) \begin{bmatrix} p \\ n \\ u \end{bmatrix}, \text{where}\, \mathbf{M}(s) = \begin{bmatrix} 0 & 0 & W_a \\ 0 & 0 & W_u \\ W_e & 0 & W_e G_0 \\ -I & -W_n & -G_0 \end{bmatrix}. \tag{36}$$

With the expression of **M**(s) in hands, the next step is to design controller $K(s)$ such that the exogenous input to controlled output transfer function $\|T_{z\omega}\|_\infty$ ($T_{z\omega}$ is the complementary sensitivity function) is minimized. However, it is difficult to find an optimal H_∞ controller since it is both numerically and theoretically complicated. In practice, a so-called sub-optimal H_∞ controller (Zhou and Doyle 1998) suit well the control goal of minimizing $\|T_{z\omega}\|_\infty$ to some degree. Utilizing the solution procedure based on maximum entropy (Zhou and Doyle 1998), a H_∞ controller of order 15 can be found with the input/output transfer function satisfying $\|T_{z\omega}\|_\infty \le 0.9617$. A model-reduction is further performed to reduce the order of the controller to 7 for easy implementation, yielding

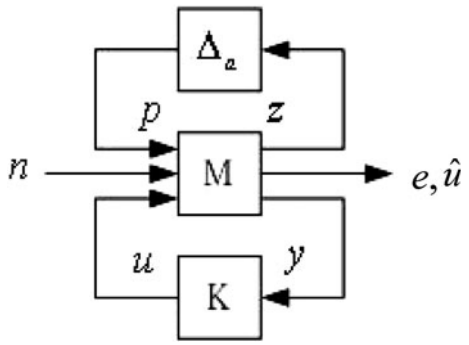

Fig. 11 LFT representation of the system

$$K(s) = \frac{56.742s^6 + 1.1028\text{e}6s^5 + 1.2854\text{e}9s^4 + 1.8534\text{e}13s^3 + 2.125\text{e}15s^2 + 7.5876\text{e}18s + 2.371\text{e}20}{s^7 + 6398.2s^6 + 3.3974\text{e}7s^5 + 1.168\text{e}11s^4 + 1.692\text{e}14s^3 + 2.601\text{e}17s^2 + 7.609\text{e}17s + 9.297\text{e}18}. \tag{37}$$

The designed H_∞ controller in Eq. 37 is ready to be implemented to the piezo-beam system, as shown in Fig. 5. Note that based on control design theory, the robustness of the controller should be examined after implementation via

$$\|W_a KS\|_\infty \le 1, \tag{38}$$

for robust stability with additive uncertainty considered (Zhou K, Doyle JC. Essentials of Robust Control, Prentice Hall: New Jersey 1998), and

$$\left\| \begin{matrix} W_e S \\ W_u KS \end{matrix} \right\|_\infty \le 1, \tag{39}$$

for robust performance. Figures 12 show comparison of frequency responses between $\{S, KS, KS\}$ and inverses of $\{1/W_e, 1/W_u, 1/W_a\}$, respectively, where it can be seen that the criteria in Eqs. 38, 39 are all satisfied with the designed controller in Eq. 37.

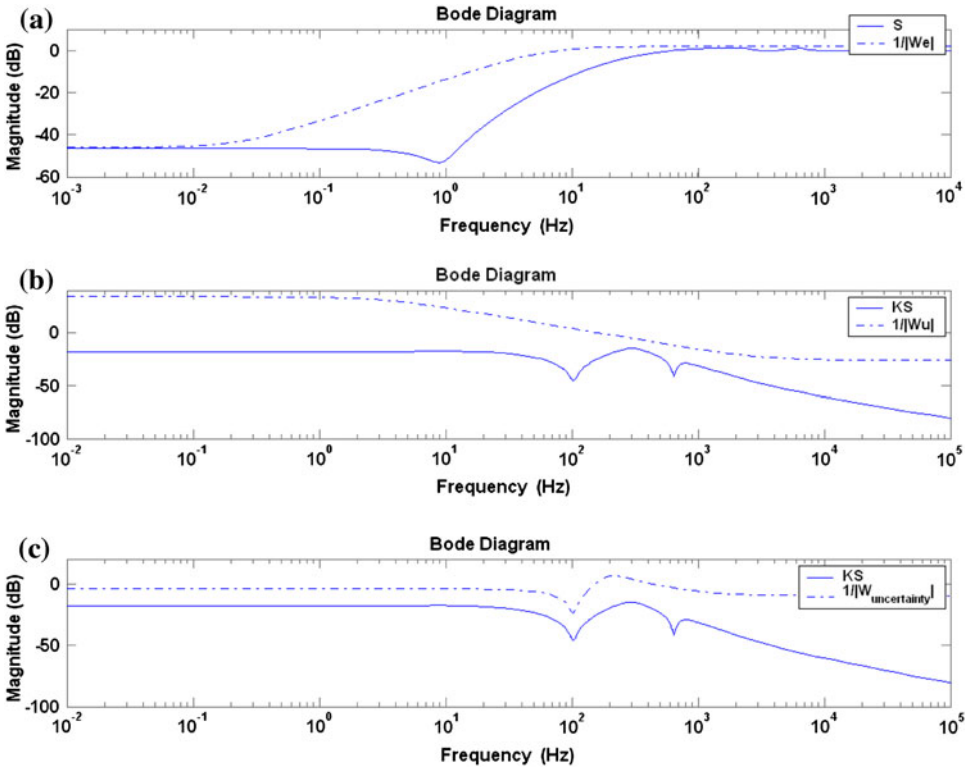

Fig. 12 Validation of robust performance and stability

7 Experimental validation

A closed-loop experimental piezo-beam system is set up with the piezoceramic patches in model no. of APC-856 (American Piezo Ceramics 1775). Figure 13 shows the experiment framework. Implementation of designed control algorithm is accomplished by the dSPACE module, which provides a 64-bit floating-point processor to minimize the computation errors associated with finite word length. Furthermore, the sampling rate of dSPACE is selected as 20 kHz, which is adequate to suppress the primary disturbance below 400 Hz due to spindle runout, the secondary around 400–1,000 Hz due to disk flutter vibration (Li and Horowitz 2002; Li et al. 2003; Huang et al. 2006), and minimize negative effects of quantization. The output control signal is amplified by a power amplifier (HAS 4051) to provide enough voltage to derive the piezoelectric beam. The motion of beam tip is measured by a laser displacement sensor (MTI 250, MICROTRAK 7000). The sensor signal is fed back to the dSPACE module for computing control output. Note that the resolution of the laser displacement is ±0.1–0.2 μm. The material properties and dimensions of the piezocreamic patches, and brass are listed in Table 1. It is pertinent to note at this point that while applied to hard disk drives with a fixed point processor, one can use available simulators off-line to emulate realistic digital computation environment; e.g., the Fixed Point Blockset, a feature of MATLAB/Simulink, to estimate errors and noise

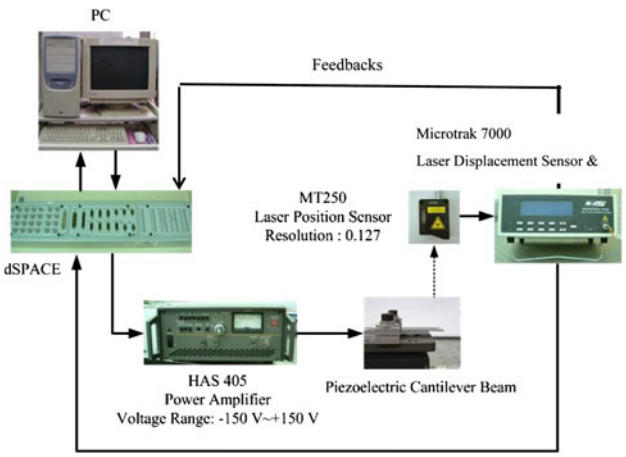

Fig. 13 Experimental setup

due to quantization and finite word length, respectively. In this way, the scaling of the controller coefficients in Eq. 37 and power/memory resources for computation in the fixed point processor can be optimized before implementation of control design.

In experiments, two types of commands—steps and sinusoids—are applied to examine controller performance. Figure 14 shows simulated and experimental responses with the designed controller (28) to perform microscopic hysteresis cancellation and the H_∞ controller in Eq. 37 to compensate the error resulted from previous hysteresis cancellation, where it is seen that both are close to each

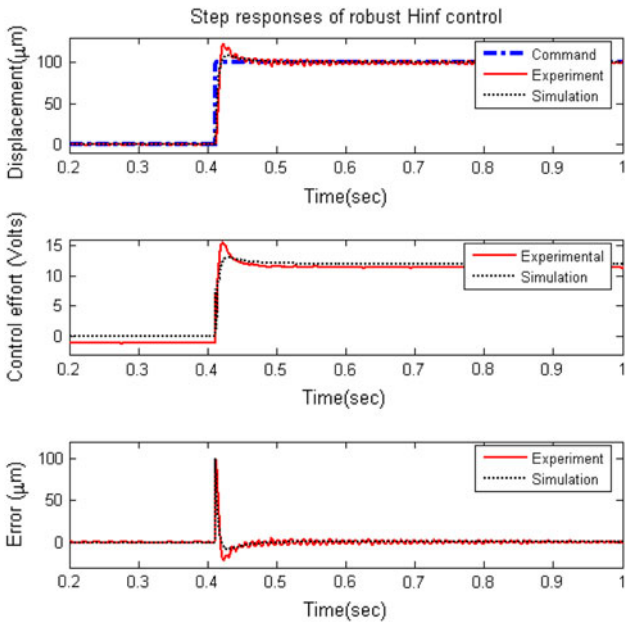

Fig. 14 Simulated and experimental step responses with the microscopic hysteresis cancellation assisted by H_∞ compensation

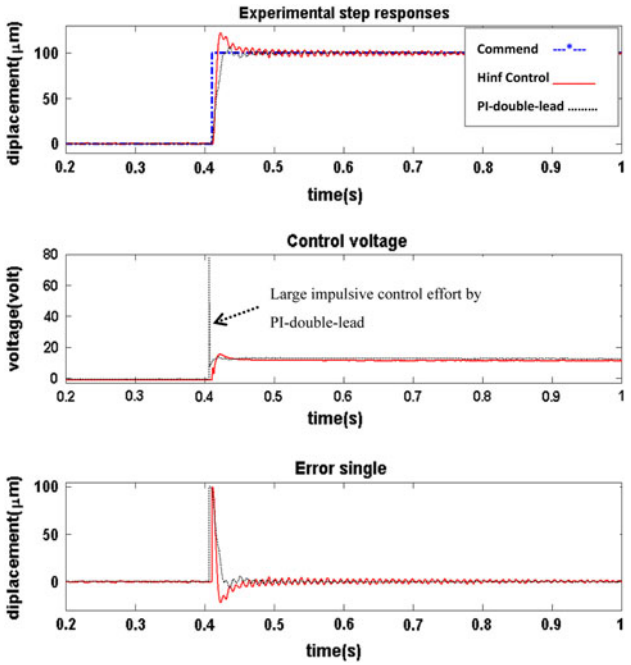

Fig. 15 Experimental step responses employing the designed H_∞ controller and PI-double-lead compensator

other and the controller successfully performs positioning within 0.05 s for a long range of 100 μm. On the other hand, Fig. 15 show experimental step responses employing the designed H_∞ controller and PI-double-lead compensator for comparison. It is seen from this figure that the H_∞ controller appears more effective with efficient control effort (not the large impulsive control effort required by PI-double-lead) as shown in subfigure (b) for achieving similar performance, as shown in subfigure (a), in terms of precision tracking at steady state and small settling time. Also, Fig. 16a, b show the steady-state results for sinusoidal commands in 1 Hz and 10 Hz, respectively. It is seen from subfigure (a) that the hysteresis cancellation with a H_∞ compensator renders much smaller positioning errors for 1 Hz command than 10 Hz. This is due to the fact that the Preisach model is originally identified based on a quasi-static process. The positioning errors would be magnified as the frequency of the sinusoidal command increases (Ben Mrad and Hu 2002).

It is pertinent to note at this point that the application of the proposed control scheme is not originally limited to hard disk drives; thus, the piezo-beam considered for experimental study as shown in Fig. 5 is in larger size, which does not exhibit clear hysteresis effects until driven to 100 μm. With this size, the bandwidth of the considered piezo-actuator is lower (around 100 Hz) than that (above 10 kHz) of the much smaller piezoelectric micro-actuators designed and used for dual-stage control in hard disk drives (Mori et al. 1991; Li and Horowitz 2002; Li et al. 2003; Huang et al. 2006; Oboe et al. 1999; Tsai and Yen 1999; Tokuyama et al. 2001; Lou et al. 2002; Gao and Swei 2000; Liu et al. 2002; Suzuki et al. 2003; Tagawa et al. 2003). It is the main reason that the experimental sinusoidal commands adopted herein are primarily around 1 and 10 Hz and up to 100 μm positioning range to exhibit hysteresis. In addition, a displacement sensor with better resolution and lower noise than the one used herein is also needed to conduct experiments to mimic the environment of hard drives. However, even though with the above limitations on the experimental study, it is for sure that since the techniques of modeling and control design proposed in this study are generic and the sampling rate of the dSPACE microprocessor is up to 20 kHz, the proposed controller can be applied to varied sizes of piezo-actuators, including the micro-sized actuators documented in (Mori et al. 1991; Li and Horowitz 2002; Li et al. 2003; Huang et al. 2006; Oboe et al. 1999; Tsai and Yen 1999; Tokuyama et al. 2001; Lou et al. 2002; Gao and Swei 2000; Liu et al. 2002; Suzuki et al. 2003; Tagawa et al. 2003). Note that the sampling rate of 20 kHz is fast enough to suppress the primary disturbance below 400 Hz due to spindle runouts and the secondary around 400–1,000 Hz due to disk flutter vibration (Li and Horowitz 2002; Li et al. 2003; Huang et al. 2006). Therefore, the same level of performance presented in this section for the larger-sized actuator is also expected for the micro-sized ones in a production hard disk drive.

In addition to the positioning technique of the proposed hysteresis cancellation and an H_∞ controller, a

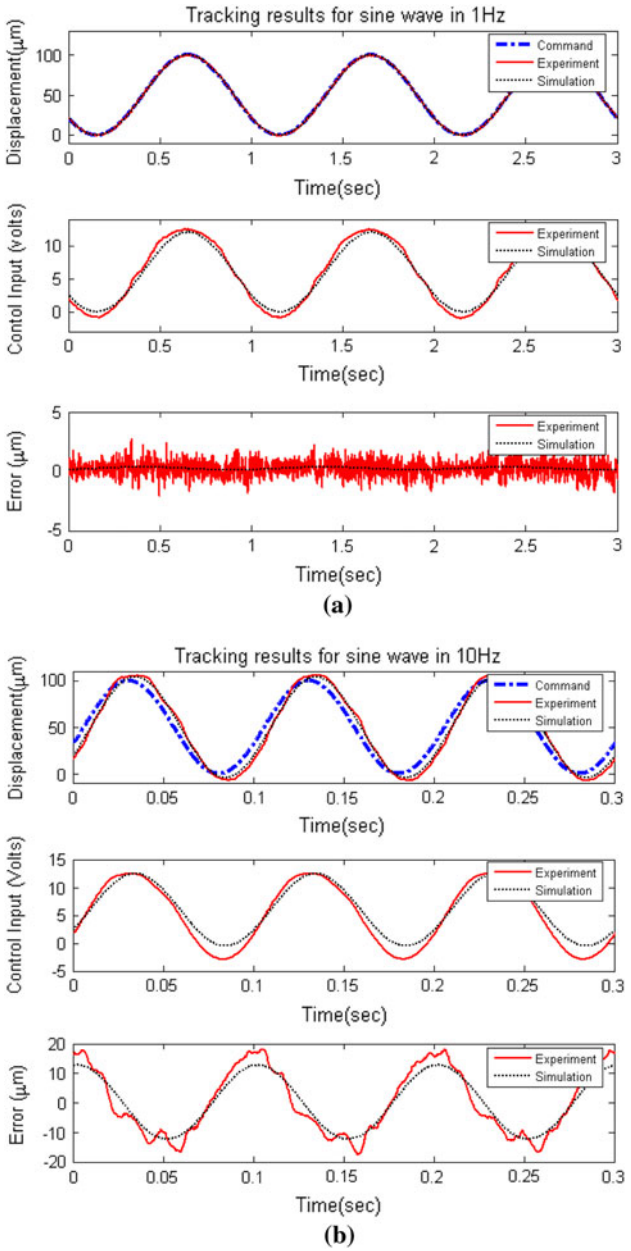

Fig. 16 Simulated and experimental tracking results for the cases with the hysteresis cancellation assisted by H_∞ compensation for sinusoidal commands in frequencies of 1 and 10 Hz

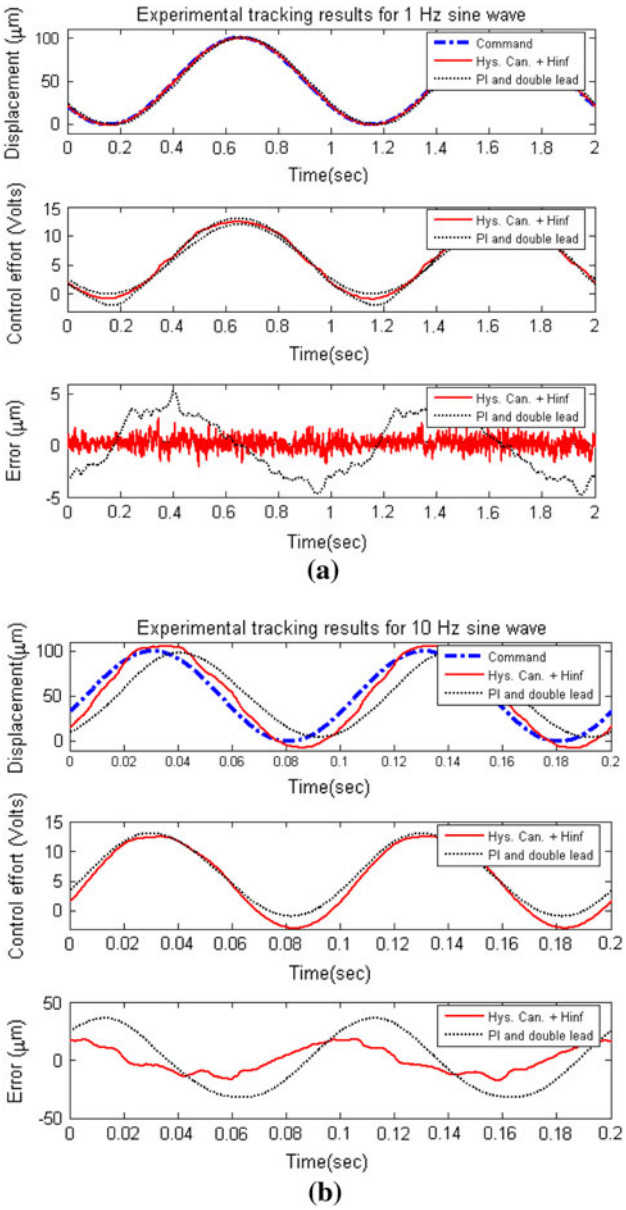

Fig. 17 Simulated and experimental tracking results for the cases with the hysteresis cancellation assisted by H_∞ and PI-double-lead compensations for sinusoidal commands in frequencies of 1 and 10 Hz

conventional, widely-used-in-industry PI and double-lead controller (Lee 2005) is designed based on the nominal plant—without considering the hysteresis term in the second equation of Eq. 4—and tested for comparison. The PI control is chosen to achieve zero steady-state error, while the double-lead to render necessary stability. Note that the aforementioned comparison aims mainly to show effectiveness of microscopic hysteresis cancellation, not determining superiority between H_∞ and PI-double-lead controllers. Figure 17 shows resulted experimental results for sinusoidal commands in 1 and 10 Hz. It is seen from these figures that the hysteresis cancellation with a robust H_∞ compensator renders a much better control performance in terms of much smaller errors for 1 Hz sinusoidal command and moderately better performance for 10 Hz command, than the PI and double-lead controller. For a clearer view on hysteresis rejection, the afore-obtained steady state simulation and experimental results are re-represented in the voltage-displacement domain in Fig. 18, as loops. It is seen from this figure that the experimental loop with 1 Hz sinusoidal command encloses a very small area and close to those simulated counterpart,

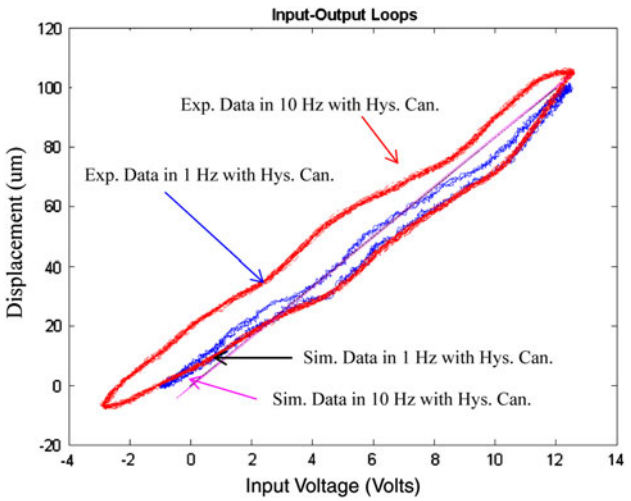

Fig. 18 Experimental and simulated steady-state voltage-displacement loops with the microscopic hysteresis cancellation assisted by robust H_∞ compensation and subjected to sinusoidal commands in frequencies 1 and 10 Hz

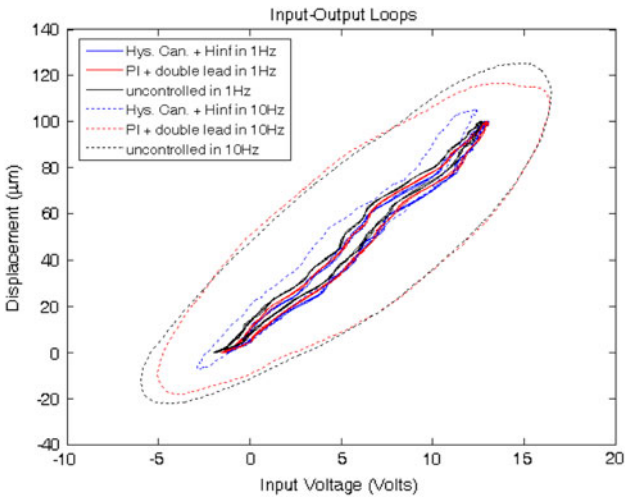

Fig. 19 Experimental results for the cases (1) with microscopic hysteresis cancellation and H_∞ compensation design, (2) with a conventional PI and double-lead compensator designed but without hysteresis cancellation, and (3) no feedback control; furthermore, the cases are subjected to sinusoidal commands in frequencies 1 and 10 Hz

while the difference between experimental and simulated is magnified due to imprecision of hysteresis modeling as subjected to faster commands. Note that both simulated loops appear with almost no enclosed area, showing excellent theoretical performance of the hysteresis cancellation with a robust H_∞ compensator. Finally, Fig. 19 shows the experimental loops for three different cases with (1) the hysteresis cancellation equipped with an H_∞ controller for compensating the resulting error; (2) a conventional PI plus double-lead control without considering hysteresis; (3) no feedback control (open-loop). It is seen from this figure that for those cases in 1 Hz, the controller (1) and (2) renders slightly smaller loop areas than (3), showing the basic effects of the feedback compensation to suppress hysteresis. As the loop command frequency increased to 10 Hz when the hysteresis effects are relative significant, the controller via the hysteresis cancellation and robust H_∞ control leads to much smaller loop areas than the other two cases, showing that the proposed control scheme indeed improves the performance substantially by canceling the hysteresis effects in the microscopic level.

8 Conclusions

This study proposes a control scheme consisting of microscopic hysteresis cancellation and an accompanied robust H_∞ controller to overcome resulted cancellation errors. The proposed modeling is novel in the addition of a polarization term into linear constitutive equations of piezoelectric materials. Preisach model is then used to describe the polarization and employ finite element modeling afterward. In this way, one is able to predict macroscopic hysteresis effects of piezoelectric structures in microscopic level. The proposed modeling and control technique is applicable to piezoelectric structures in complicated geometry and varied sizes. Simulation and experiment are conducted to validate controller performance. The conclusive remarks based on the simulations and experimental results are summarized as follows.

1. The microscopic polarization is successfully modeled by Preisach model and further identified via the built finite element model. In identification, a quasi-static process of voltage application is employed. The obtained prediction errors are within acceptable 3% in percentage.
2. For step commands, simulated and experimental responses with the hysteresis cancellation assisted by a robust H_∞ compensator are close to each other with non-notable positioning error within 0.05 s, even for a long range of 100 μm.
3. For sinusoidal commands, the designed hysteresis cancellation assisted by a robust H_∞ compensator renders much smaller positioning errors for 1 Hz command than 10 Hz. This is due to the fact that the Preisach model is originally identified based on a quasi-static process. The positioning errors would be magnified as the frequencies of sinusoidal commands increase.
4. Compared to the conventional PI and double-lead controller without hysteresis cancellation, the proposed microscopic hysteresis cancellation and a H_∞

compensator renders much better control performance for 10 Hz, showing that the proposed control scheme improves the performance substantially by canceling the hysteresis effects in the microscopic level.

In the future, the identification on polarization would be performed following non-quasi-static processes, i.e. considering dynamic applied voltage, to reflect effects of dynamic hysteresis effects. Furthermore, the proposed control design would be applied to micro-sized actuators in production hard disk drives.

Acknowledgments The authors are indebted to the National Science Council of ROC for the financial support through the contacts NSC 95-2221-E-009-367, NSC 95-2745-E-033-004-URD, and NSC 97-2221-E-009-057-MY3. The authors are also grateful to National Chip Implementation Center (CIC) of Taiwan for help implement the controllers. This work was supported in part by the National Science Council, Taiwan, on Establishing "International Research-Intensive Centers of Excellence in Taiwan" (IRiCE Project) under Contract NSC 99-2911-I-010-101, and in part by the Aiming for the Top University Plan of National Chiao Tung University, the Ministry of Education, Taiwan, under Contract 99W962.

References

American Piezo Ceramics, Inc. Standard stripe actuator product specifications Mackeyville, Pennsylvania 17750-0180m, USA

Andronikou A, Bekeym A, Hadaegh FY (1983) Identification of nonlinear systems with hysteretic elements. J Dyn Sys Meas Control 105(4):209–214

Ben Mrad R, Hu H (2002) A model for voltage-to-displacement dynamics in piezoceramic actuators subject to dynamic-voltage excitations. IEEE Trans Mech 7(4):479–489

Chen P, Montgomery S (1980) A macroscopic theory for the existence of the hysteresis and butterfly loops in ferroelectricity. Ferrroelectrics 23:199–207

Chen IW, Wang Y (1998) A domain wall model for relaxor ferroelectrics. Ferroelectrics 206:245–263

Dong R, Tan Y (2009) A modified Prandtl–Ishlinskii modeling method for hysteresis. Phys B 404:1336–1342

Freeman AR, Joshi SP (1995) Numerical modeling of PZT nonlinear electromechnaical behavior. SPIE Proc 2715:602–613

Gao P, Swei SM (2000) Active actuation and control of a miniaturized suspension structure in hard-disk drives using a polyvinylidene-fluoride actuator and sensor. Meas Sci Technol 11:89–94

Ge P, Jouaneh M (1995) Modeling hysteresis in piezoceramic actuators. Precis Eng 17:211–221

Huang X, Nagamune R, Horowitz R (2006) A comparison of multirate robust track-following control synthesis techniques for dual-stage and multisensing servo systems in hard disk drives. IEEE Trans Magn 42(7):932–937

Hughes D, Wen JT (1995) Preisach modeling of piezoceramic and shape alloy hysteresis. SPIE Proc 2715:507–528

Hutton RS (2009) Modeling the united states unemployment rate with the Preisach model of hysteresis. Virginia Polytechnic Institute and State University 2009, Virginia

Janaideh AE, Feng Y, Rakheja S, Su CY, Rabbath CA (2009) Hysteresis compensation for smart actuators using inverse generalized Prandtl–Ishlinskii model. In: Proceedings of 2009 American control conference, St. Louis, MO, USA, June 10–12, 2009, pp 307–312

Kim SH, Kim JH, Yang J, Yang H, Park JY, Park YP (2009) Tilt detection and servo control method for the holographic data storage system. Microsyst Technol 15:1695–1700

Lee LK (1979) Piezoelectric bimorph optical beam scanners: analysis and construction. Appl Opt 18:454–459

Lee GY (2005) Design of autotuning algorithms for the piezoelectric pickups and experimental verification. Master thesis, Chung Yuan University, Chung-Li, Taiwan

Li Y, Horowitz R (2002) Design and testing of track-following controllers for dual-stage servo systems with PZT actuated suspensions. Microsyst Technol 8:194–205

Li Y, Horowitz R, Evans R (2003) Vibration control of a PZT actuated suspension dual-stage servo system using a PZT sensor. IEEE Trans Magn 39(2):194–205

Liu X, Li A, Clegg W, Jenkins DFL, Davey P (2002) Head-disk spacing variation suppression via active flying height control. IEEE Trans Instrum Meas 51(5):897–901

Lou Y, Gao P, Qin B, Guo G, Ong EH, Takada A, Okada K (2002) Dual-stage servo with on-slider PZT microactuator for hard disk drives. IEEE Trans Magn 38(5):2183–2185

Mayergoyz ID (1991) Mathematical models of hysteresis. Springer, New York

Mori K, Munemoto T, Otsuki H, Yamaguchi Y, Akagi K (1991) A dual-stage magnetic disk drive actuator using a piezoelectric device for a high track density. IEEE Trans Magn 27(6): 5298–5300

Newcomb C, Flinn I (1982) Improving the linearity of piezoelectric ceramic actuators. Elec Let 18:442–444

Oboe R, Beghi A, Murari B (1999) Modeling and control of a dual stage actuator hard disk drive with piezoelectric secondary actuator. In: Proceedings of the 1999 IEEE/ASME international conference on advanced intelligent mechatronics, Atlanta, USA, pp 138–143

Peng J, Chao C, Tang H (2010) Piezoelectric micro machined ultrasonic transducer based on dome-shaped piezoelectric single layer. Microsyst Technol 16:1771–1775

Preisach F (1935) Uber die mognetidche nachwirkung. Z Phys 94:277–302

Rao SS (1986) Mechanical vibrations, Addison-Wesley, New York

Shaffer JJ, Fried DL (1970) Bender-bimorph scanner analysis. Appl Opt 9:933–937

Simkovics R, Landes H, Ka1tenbacher M, Hoffelner J, Lerch R (2000) Finite element analysis of hysteresis effects in piezoelectric transducers. Proc SPIE Int Soc Opt Eng 3984:33–44

Suzuki K, Maeda R, Jiaru Chu, Kato T, Kurita M (2003) An active head slider using a piezoelectric cantilever for in situ flying-height control. IEEE Trans Magn 39(2):826–831

Tagawa N, Kitamura KI, Mori A (2003) Design and fabrication of MEMS-based active slider using double-layered composite PZT thin film in hard disk drives. IEEE Trans Magn 39(2):926–931

Tokuyama M, Toshihiko S, Hiromitsu M, Nakamura S, Hanya M, Osamu I, Soga J (2001) Development of a Φ-shaped actuated suspension for 100-kTPI hard disk drives. IEEE Trans Magn 37(4):1884–1886

Tsai KY, Yen JY (1999) Servo system design of a high-resolution piezo-driven fine stage for step-and-repeat microlithography systems. In: Proceedings of IECON (Industrial Electronics Conference), San Jose, CA, USA, pp 11–16

Yu Y, Naganathan N, Dukkipati R (2002) Preisach modeling of hysteresis for piezoceramic actuator system. Mech Mach Theory 37(1):49–59

Zhou K, Doyle JC (1998) Essentials of robust control, Prentice Hall, New Jersey